Article

Path Tracking Control with Constraint on Tire Slip Angles under Low-Friction Road Conditions

Jaepoong Lee [1] and Seongjin Yim [2,*]

1   Department of Intelligent Systems and Robotics, Chungbuk National University, Cheongju 28644, Chungbuk, Republic of Korea; ske03005@chungbuk.ac.kr
2   Research Center for Electrical and Information Technology, Seoul National University of Science and Technology, 232 Gongneung-ro, Nowon-gu, Seoul 01811, Republic of Korea
*   Correspondence: acebtif@seoultech.ac.kr; Tel.: +82-2-970-9011

Featured Application: Path Tracking Control for Autonomous Driving.

Abstract: This paper presents a method to design a path tracking controller with a constraint on tire slip angles under low-friction road conditions. On a low-friction road surface, a lateral tire force is easily saturated and decreases as a tire slip angle increases by a large steering angle. Under this situation, a path tracking controller cannot achieve its maximum performance. To cope with this problem, it is necessary to limit tire slip angles to a value where the maximum lateral tire force is achieved. The most commonly used controllers for path tracking, linear quadratic regulator (LQR) and model predictive control (MPC), are adopted as a controller design methodology. The control inputs of LQR and MPC are front and rear steering angles and control yaw moment, which have been widely used for path tracking. The constraint derived from tire slip angles is imposed on the steering angles of LQR and MPC. To fully verify the performance of the path tracking controller with the constraint on tire slip angles, a simulation is conducted on vehicle simulation software. From the simulation results, it is shown that the path tracking controller with the constraint on tire slip angles presented in this paper is quite effective for path tracking on low-friction road surface.

Keywords: path tracking control; low-friction road condition; tire slip angle; tire force saturation

1. Introduction

Over the past decade, research groups and the automobile industry have intensively explored autonomous driving because it is predicted to have impacts on several aspects of driving such as traffic flow, ride comfort, and road safety [1–3]. With respect to safety, autonomous driving has been expected to reduce social costs and damages incurred from drivers by preventing traffic accidents. As a result, a huge amount of papers on autonomous driving have been published in the meantime. According to the survey, it has been widely known that autonomous driving operations include perception, localization, planning, control and navigation, and system management [3]. Among them, planning or path planning generates a reference or target path based on information obtained from environments, and path tracking controls a vehicle, following the reference states with several actuators. This paper focuses on path tracking control (PTC). For the last decade, PTC has been intensively explored [4–6]. Consequently, a huge deal of papers have been published to date in the field of PTC [4–10].

To date, most path tracking controllers for autonomous driving have been designed on a high-friction road surface where the tire-road friction coefficient, μ, was set between 0.8 and 1.0. Since 2019, some papers concentrating on PTC under low-friction road conditions have been published [11–32]. These papers are classified according to controller design methodologies, input configurations, actuator combinations and tire-road friction

coefficient, as given in Table 1. As shown in Table 1, the lower limits of μ were set between 0.25 and 0.4. In this paper, a low friction road condition means that μ is 0.4 or less.

Table 1. Summary of path tracking controllers on low friction roads.

Controller	Input Configuration	Actuators	μ	Reference
LQR, MPC, SMC	$[\delta_f]$, $[\delta_f\ \delta_r]$	FWS, 4WS	0.4	[30]
MPC	$[\delta_f]$	FWS	0.4, 0.5 0.2, 0.5 0.3, 0.8 0.2, 0.85 0.3	[12] [14] [15] [21] [22]
MPC	$[\delta_f\ \Delta F_x]$	FWS, 4WID FWS, 4WID, 4WIB FWS, 4WID, 4WIB FWS, 4WIB	0.4, 0.5 0.6, 0.7 0.4, 0.8 0.3	[11] [16] [17] [28]
MPC	$[\delta_f]$ $[\delta_f\ \Delta F_x\ \Delta M_z]$ $[\delta_f]$, $[\Delta M_z]$ $[\delta_f\ \Delta M_z]$	FWS, 4WID FWS, 4WID FWS, 4WID, 4WIB FWS, 4WID	0.4,0.7 0.3 0.3 0.5, 0.6	[19] [20] [23] [29]
LQR	$[\delta_f\ \delta_r]$ $[\delta_f\ \delta_r]$ $[\delta_f]$	4WS, 4WIS 4WS FWS	0.4, 0.65 0.25, 0.5 0.34	[13] [18] [24]
LQR	$[\delta_f]$, $[\delta_f\ \delta_r]$, $[\delta_f\ \delta_r$ $\Delta M_z]$	FWS, 4WS, 4WIB, 4WID	0.4	[31,32]
SMC	$[\Delta M_z]$ $[\delta_f]$ $[\delta_f\ \Delta M_z]$	4WIS, 4WID, 4WIB FWS FWS, 4WID, 4WIB	0.4 0.5 0.3	[25] [26] [27]

In Table 1, δ_f, δ_r, ΔF_x and ΔM_z are the control inputs, which represent the front and rear steering angles, the control longitudinal force, and the control yaw moment, respectively. An input configuration is composed of those control inputs. In Table 1, seven input configurations were given. With those input configurations, a linear quadratic regulator (LQR), model predictive control (MPC), and sliding mode control (SMC) were adopted as a controller design methodology.

From the point of view of an actuator for PTC, front wheel steering (FWS), rear wheel steering (RWS) and 4-wheel steering (4WS) have been selected as an actuator for PTC to date. For the last decade, by virtue of development of in-wheel motor or e-corner module systems, 4-wheel independent steering/braking/driving (4WIS/4WIB/4WID) has been available for vehicle stability control (VSC) and PTC. Several actuator combinations can be composed of those actuators, as shown in Table 1. If ΔM_z or ΔF_x is selected as a control input, a control allocation is needed to distribute it the control tire forces generated by RWS, 4WID and 4WIB.

Naturally, on a low-friction road surface, the magnitudes of longitudinal and lateral tire forces, F_x and F_y, become small because μ is low [33,34]. Among them, F_y's generated at front wheels have significant effects on path tracking performance in cornering. Figure 1 shows F_y with respect to the tire slip angle, α, and μ. In Figure 1, the values of the tire slip angles, α_m and α_∞, are 5° and 20°, which give the maximum and saturated lateral tire forces, $F_{y,max}$ and $F_{y,\infty}$, respectively. As shown in Figure 1, F_y is saturated and decreased to $F_{y,\infty}$ as α increases to α_∞ over α_m where $F_{y,max}$ is generated. In other words, F_y becomes $F_{y,\infty}$, which is smaller than $F_{y,max}$ due to larger slip angle α_∞ over α_m. For example in Figure 1, 16% of $F_{y,max}$ is reduced at α_∞ when μ is 0.6. Moreover, F_y is reduced as μ decreases, as shown in Figure 1. On a low-friction road surface, F_y is more easily saturated than on high-friction one. For the above two reasons, a path tracking controller, designed on a

high-friction road surface, shows a poor performance on a low-friction one. To overcome this problem, it is necessary to design a path tracking controller with the consideration of low-friction road surface and lateral tire force saturation. In this paper, a constraint on the tire slip angle (CTSA) is derived from the definition of α, which results in the bound constraint on steering angles.
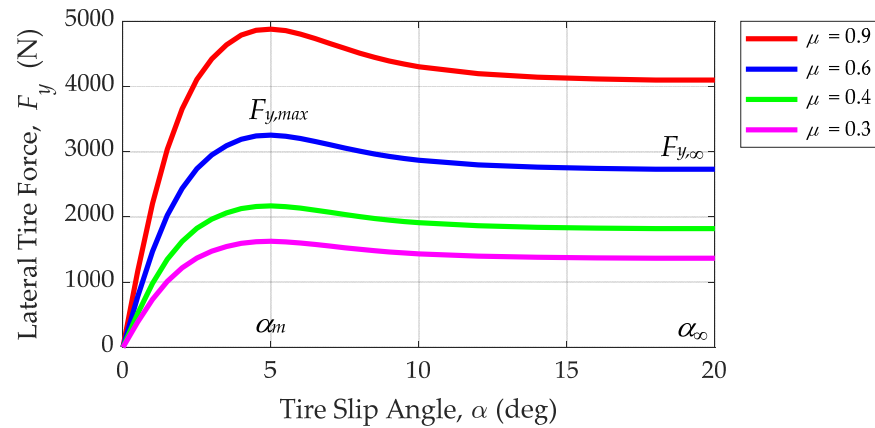

Figure 1. F_y with respect to α and μ.

Research on vehicle motion control under low-friction road conditions has been performed in the field of vehicle stability control (VSC). In this paper, VSC means a control which tries to make a vehicle track a reference yaw rate generated by a steering angle, and lateral stability control (LSC) means a control which tries to keep the side-slip angle, β, as small as possible [34,35]. To date, a lot of papers have been published in the field of VSC and LSC [36–38]. Among the literature, some papers have been published to limit the tire slip angle such that F_y is not saturated or F_y is maintained at its maximum on low-friction road surface [39–45].

These papers can be classified into two categories. The first approach is to limit the slip angle of the front wheel when α is over α_m at control allocation stage [39,40]. If F_y reaches its maximum, then the optimization variable F_y of front wheel is set to the constant $F_{y,max}$, and an extra optimization problem is formulated with remaining variables and modified cost function. Generally, quadratic programming (QP) has been adopted for control allocation. In the research, QP is applied twice so as to limit α. Another method is to use a daisy chaining method (DCM) for control allocation, which is a cascade optimization under element-wise constraint [41]. The second approach is to use an extra controller for the purpose of making α be α_m [42–45]. In the research, various methods have been applied to keep F_y at its maximum so as to generate the maximum lateral acceleration. For example, some compensation coefficients were adopted to tune the magnitude of $F_{y,max}$. However, in these research projects, α was not directly manipulated by a method. Different from the previous two research projects, CTSAs are set as the bound on steering angles in this paper.

The aim of this paper is to present a method to impose a CTSA for the purpose of making a path tracking controller better under low friction conditions. From the definition of tire slip angle, CTSA is derived. To consider CTSA in controller design procedure, LQR and MPC are adopted as a controller design methodology. δ_f and δ_r and ΔM_z are selected as a control input, which make three input configurations. When imposing CTSA in LQR, the control inputs, δ_f and δ_r, are clipped by the constraint. In MPC, the constraint on steering angle is simply added into the optimization procedure. To distribute ΔM_z into tire forces generated by various actuator combinations, a control allocation is applied. Through the control allocation, the effects of various actuator combinations composed from FWS, 4WS, 4WID and 4WIB, on path tracking performance is analyzed. A simulation is done on a vehicle simulation software, CarSim 8.02, to verify path tracking performance with CTSAs. From simulation results, it is concluded that a path tracking controller with CTSA shows

quite a better performance in terms of path tracking than one without CTSA on low-friction road surface.

The contributions of this paper can be summarized as follows:

1. This paper presents a method to impose a CTSA on steering angles in order to generate the maximum lateral force on a low-friction road surface. The constraint is simply derived from the definition of tire slip angle and easily applied into steering angles, i.e., control inputs of LQR and MPC. From simulation results, it is verified that the CTSA can greatly improve the path tracking performance on low-friction surface.

2. The proposed CTSA makes the most of the lateral tire force. This means that there are little tire forces left to improve the control performance with extra actuators. Under that condition, the effects of various combinations composed from the actuators such as RWS, 4WID, and 4WIB on control performance are discussed from simulation results.

3. From the discussion on simulation results, it is recommended that LQR is better than MPC in terms of computation time and simplicity of controller structure, and that the actuator combination, FWS + RWS, shows the best performance under CTSA.

This paper consists of five sections. In Section 2, design procedures for LQR and MPC with various actuator combinations are presented. Moreover, the derivation procedure for CTSAs is also presented. In Section 3, performance measures on path tracking are presented for the purpose of tuning LQR and MPC. In Section 4, simulation is conducted and simulation results are discussed in view of the performance measures. The conclusion of this paper is drawn in Section 5.

2. Design of Path Tracking Controller with Constraints on Tire Slip Angles

2.1. Vehicle Model

In the context of PTC, a 2-DOF bicycle model has been widely employed to represent yaw and lateral behaviors of a vehicle, as discussed in the literature [25,30–35,39,40]. Figure 2 shows the coordinates, geometry, and variables of the bicycle model. This models the lateral and yaw motions of a vehicle under the assumption of a constant longitudinal velocity. The state variables for this model are the yaw rate, γ, and the side-slip angle, β. With these variables, the equations of motion (1) are obtained [32]. The tire slip angles, denoted as α_f and α_r, are defined as Equation (2) for the front and rear wheels. The linear lateral tire forces, F_{yf} and F_{yr}, are calculated as Equation (3). By combining Equations (1)–(3), the state-space equation for the bicycle model is derived as Equation (4).
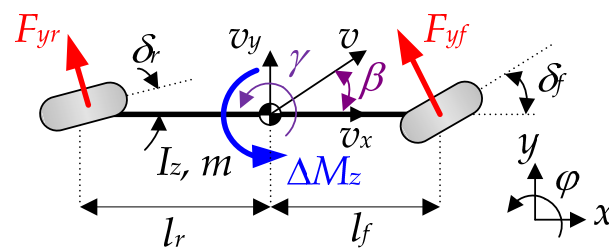
Figure 2. 2-DOF dynamic bicycle model.

$$\begin{cases} mv_x\left\{\dot{\beta}(t) + \gamma(t)\right\} = F_{yf}(t) + F_{yr}(t) \\ I_z\dot{\gamma}(t) = l_f F_{yf}(t) - l_r F_{yr}(t) + \Delta M_z(t) \end{cases} \tag{1}$$

$$\alpha_f(t) = \delta_f(t) - \beta(t) - \frac{l_f\gamma(t)}{v_x}, \ \alpha_r(t) = \delta_r(t) - \beta(t) + \frac{l_r\gamma(t)}{v_x} \tag{2}$$

$$F_{yf}(t) = C_f\alpha_f(t), \ F_{yr}(t) = C_r\alpha_r(t) \tag{3}$$

$$\dot{\beta}(t) = \left(-\frac{C_f + C_r}{mv_x}\right)\beta(t) + \left(\frac{-C_f l_f + C_r l_r}{mv_x^2} - 1\right)\gamma(t) + \frac{C_f}{mv_x}\delta_f(t) + \frac{C_r}{mv_x}\delta_r(t)$$

$$\dot{\gamma}(t) = \left(\frac{-C_f l_f + C_r l_r}{I_z}\right)\beta(t) + \left(-\frac{l_f^2 C_f + l_r^2 C_r}{I_z v_x}\right)\gamma(t) + \frac{l_f C_f}{I_z}\delta_f(t) - \frac{l_r C_r}{I_z}\delta_r(t) + \frac{1}{I_z}\Delta M_z(t) \tag{4}$$

Figure 3 shows the coordinates and variables derived from the target path for path tracking. The literature on PTC introduced the concepts of lateral offset and heading errors, denoted as e_y and e_φ, at a specific point *C* as depicted in Figure 3 [11–32]. To enhance path tracking performance, this paper introduces a preview function, as used in the previous works [24,26,30–32]. The preview distance, L_p, is calculated using Equation (5), where k_v is the velocity gain representing the preview interval. In Figure 3, the point C is located at the vehicle's center of gravity. The preview point, *P*, and the point *Q* on the target path are determined with L_p. At the point *Q*, the time derivatives of e_y and e_φ are calculated as Equation (6), under the assumption that e_φ is limited to an angle less than 10 degrees and, consequently, can be approximated as $\sin e_\varphi \approx e_\varphi$.

$$L_p = k_v \cdot v_x \tag{5}$$

$$\begin{cases} \dot{e}_y(t) = v_x \sin e_\varphi(t) - v_x \beta(t) - L_p \gamma(t) \approx v_x e_\varphi(t) - v_x \beta(t) - L_p \gamma(t) \\ \dot{e}_\varphi(t) = \dot{\varphi}_d(t) - \dot{\varphi}(t) = v_x \chi(t) - \gamma(t) \end{cases} \tag{6}$$
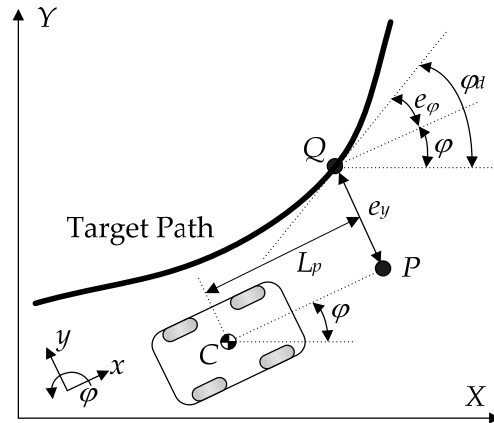

Figure 3. Coordinates and variables derived from target path.

The vectors **x**, **w**, and **u** of the states, the disturbances, and control inputs are defined as Equation (7), respectively [11,12,14–17,19–23,28,29,31,32]. With those vectors and Equations (4), (6) and (7), the state–space equation for PTC is derived as Equation (8), where the matrices **A**, $\mathbf{B}_1$ and $\mathbf{B}_2$ are defined as Equation (9) [32].

$$\begin{cases} \mathbf{x}(t) = \begin{bmatrix} e_y(t) & e_\varphi(t) & \beta(t) & \gamma(t) \end{bmatrix}^T \\ \mathbf{w}(t) = \chi(t) \\ \mathbf{u}(t) = \begin{bmatrix} \delta_f(t) & \delta_r(t) & \Delta M_z(t) \end{bmatrix}^T \end{cases} \tag{7}$$

$$\dot{\mathbf{x}}(t) = \mathbf{A}\mathbf{x}(t) + \mathbf{B}_1 \mathbf{w}(t) + \mathbf{B}_2 \mathbf{u}(t) \tag{8}$$

$$\mathbf{A} = \begin{bmatrix} 0 & v_x & -v_x & -L_p \\ 0 & 0 & 0 & -1 \\ 0 & 0 & -\frac{C_f + C_r}{mv_x} & \frac{-C_f l_f + C_r l_r}{mv_x^2} - 1 \\ 0 & 0 & \frac{-C_f l_f + C_r l_r}{I_z} & -\frac{l_f^2 C_f + l_r^2 C_r}{I_z v_x} \end{bmatrix}, \quad \mathbf{B}_1 = \begin{bmatrix} 0 \\ v_x \\ 0 \\ 0 \end{bmatrix}, \quad \mathbf{B}_2 = \begin{bmatrix} 0 & 0 & 0 \\ 0 & 0 & 0 \\ \frac{C_f}{mv_x} & \frac{C_r}{mv_x} & 0 \\ \frac{l_f C_f}{I_z} & -\frac{l_r C_r}{I_z} & \frac{1}{I_z} \end{bmatrix} \tag{9}$$

Three types of control input, named $\mathbf{u}_1$, $\mathbf{u}_2$ and $\mathbf{u}_3$, corresponding to input configurations *IC#1*, *IC#2* and *IC#3*, are composed of three elements, δ_f, δ_r and ΔM_z, as given in Equation (10) [31,32]. In Equation (10), $\mathbf{B}_2\{k\}$ representing the *k*-th column of the matrix $\mathbf{B}_2$. In Equation (10), δ_f is available in all input configurations, while δ_r is exclusively selected in

IC#2 and *IC#3*. In the case of *IC#3*, RWS, 4WIB and 4WID are used to generate ΔM_z. With those actuators, δ_r and the braking and traction torques (T_{Bi} and T_{Di}) for each wheel are obtained from ΔM_z. This paper assumes that T_{Bi} and T_{Di} are generated through the use of 4WIB and 4WID, respectively.

$$\begin{cases} \mathbf{u}_1(t) = \delta_f(t) & \mathbf{B}_{21} = [\mathbf{B}_2\{1\}] & \text{for } IC\#1 \\ \mathbf{u}_2(t) = \left[\delta_f(t)\ \delta_r(t)\right]^T & \mathbf{B}_{22} = [\mathbf{B}_2\{1\}\quad \mathbf{B}_2\{2\}] & \text{for } IC\#2 \\ \mathbf{u}_3(t) = \left[\delta_f(t)\ \Delta M_z(t)\right]^T & \mathbf{B}_{23} = [\mathbf{B}_2\{1\}\quad \mathbf{B}_2\{3\}] & \text{for } IC\#3 \end{cases} \tag{10}$$

2.2. Design of LQR

When designing LQR, a linear quadratic cost function (LQCF) is to be defined. LQCFs, J_1, J_2 and J_3, for PTC with three input configurations, *IC#1*, *IC#2*, and *IC#3*, are defined as Equation (11), respectively. These LQCFs are transformed into the vector-matrix form as Equation (12). The weighting matrices $\mathbf{Q}$ and $\mathbf{R}_i$ in Equation (12) are defined in Equation (13). The weight ρ_i in LQCFs is determined with Bryson's rule, as given in Equation (14), where ξ_i represents the maximum allowable value for the associated terms [31,32,46]. For better path tracking performance, ξ_i and k_v are tuned. The control inputs $\mathbf{u}_1$, $\mathbf{u}_2$ and $\mathbf{u}_3$ for *IC#1*, *IC#2* and *IC#3* are obtained as Equation (15). In Equation (15), $\mathbf{P}_i$ stands for the solution to the Riccati equation for *IC#i*.

$$J_0 = \int_0^\infty \left\{ \rho_1 e_y^2(t) + \rho_2 e_\varphi^2(t) + \rho_3 \beta^2(t) + \rho_4 \gamma^2(t) \right\} dt$$

$$\begin{cases} J_1 = J_0 + \int_0^\infty \left\{ \rho_5 \delta_f^2(t) \right\} dt & \text{for } IC\#1 \\ J_2 = J_0 + \int_0^\infty \left\{ \rho_5 \delta_f^2(t) + \rho_6 \delta_r^2(t) \right\} dt & \text{for } IC\#2 \\ J_3 = J_0 + \int_0^\infty \left\{ \rho_5 \delta_f^2(t) + \rho_7 \Delta M_z^2(t) \right\} dt & \text{for } IC\#3 \end{cases} \tag{11}$$

$$J_i = \int_0^\infty \begin{bmatrix} \mathbf{x}(t) \\ \mathbf{u}_i(t) \end{bmatrix}^T \begin{bmatrix} \mathbf{Q} & \mathbf{0} \\ \mathbf{0} & \mathbf{R}_i \end{bmatrix} \begin{bmatrix} \mathbf{x}(t) \\ \mathbf{u}_i(t) \end{bmatrix} dt, \ i = 1, 2, 3 \tag{12}$$

$$\mathbf{Q} = diag(\rho_1, \rho_2, \rho_3, \rho_4), \begin{cases} \mathbf{R}_1 = \rho_5 & \text{for } IC\#1 \\ \mathbf{R}_2 = diag(\rho_5, \rho_6) & \text{for } IC\#2 \\ \mathbf{R}_3 = diag(\rho_5, \rho_7) & \text{for } IC\#3 \end{cases} \tag{13}$$

$$\rho_i = \frac{1}{\xi_i^2} \tag{14}$$

$$\mathbf{u}_i(t) = -\mathbf{K}_i \mathbf{x}(t) = -\mathbf{R}_i^{-1} \mathbf{B}_{2i}^T \mathbf{P}_i \mathbf{x}(t), \ i = 1, 2, 3 \tag{15}$$

2.3. Constraint on Tire Slip Angles

Generally, there are physical limits on the front and rear steering angles, δ_f and δ_r. For example, δ_f and δ_r are limited to 30° and 5°, respectively. Under the limitations, δ_f is easily saturated on a low-friction road surface [33,34]. Moreover, as shown in Figure 1, F_{yf} is also saturated and decreased as α_f is over α_m where $F_{y,max}$ is generated. In case of that condition, a path tracking controller cannot achieve the maximum performance. For the reason, α should be limited to α_m, as given in Equation (16). By combining Equation (2) and Equation (16), Equation (17) is obtained. From Equation (17), the constraints on α_f and α_r are obtained as Equation (18). Let this denote the constraint on the tire slip angle, Equation (18), as CTSA.

$$\left|\alpha_f(t)\right| \leq \alpha_m, \ |\alpha_r(t)| \leq \alpha_m \tag{16}$$

$$\left|\alpha_f(t)\right| = \left|\delta_f(t) - \beta(t) - \frac{l_f \gamma(t)}{v_x}\right| \leq \alpha_m, \ |\alpha_r(t)| = \left|\delta_r(t) - \beta(t) + \frac{l_r \gamma(t)}{v_x}\right| \leq \alpha_m \tag{17}$$

$$\begin{cases} -\alpha_m + \beta(t) + \frac{l_f \gamma(t)}{v_x} \leq \delta_f(t) \leq \alpha_m + \beta(t) + \frac{l_f \gamma(t)}{v_x} \\ -\alpha_m + \beta(t) - \frac{l_r \gamma(t)}{v_x} \leq \delta_r(t) \leq \alpha_m + \beta(t) - \frac{l_r \gamma(t)}{v_x} \end{cases} \tag{18}$$

In order to calculate the lower and upper bounds of Equation (18), it is essential to measure or estimate β. However, β is hard to measure with an on-board sensor. For this reason, β should be estimated with an observer. For the purpose, an extended Kalman Filter is employed in this paper [47].

From the point of view of LQR, Equation (18) is the constraint on the control inputs, δ_f and δ_r. For this reason, it is necessary to design LQR with the consideration of the constraints. The simplest way to impose the constraints, Equation (18), is to clip the control inputs obtained from LQR with the constraints. This does not need any additional procedures. The second method is to design with LQR under the constraints, Equation (18). The third method is to use MPC because it can explicitly handle any constraints in optimization procedure. The second method is not considered in this paper. Let this denote LQR without and with the CTSA as LQRN and LQRC, respectively.

2.4. Design of MPC with Constraints on Tire Slip Angles

As shown in Table 1, MPC has been widely adopted as a path tracking controller for the last decade because it can handle nonlinear or time-varying systems and nonlinear constraints besides linear time-invariant ones [11,12,14,16,17,19–22,27–30]. Generally, MPC is designed in the discrete-time domain. For the reason, the first step of MPC is to discretize Equation (8) with the sampling time, T_s. As a result, the discrete–time version of Equation (8) is obtained as Equation (19). In Equation (19), the subscript k represents a particular time instant. If k is 0, it means the current time instant. The matrices **F**, **G** and **H** in Equation (19) are obtained as an approximated form of Equation (20). In this paper, it is assumed that the disturbance $\mathbf{w}_k$ in Equation (19) is set to 0. The discrete–time version of LQCF, Equation (11), is obtained as Equation (21). In Equation (21), N is the prediction horizon. Let this denote the current state vector as $\mathbf{x}_0$. The state vector at the time instant k is obtained as Equation (22) from Equation (19). In Equation (22), $\mathbf{x}_0$ is the current state. By expanding Equation (22) from the first to N-th time instant, new vectors and matrices are defined as Equation (23). With these definitions, the state–space equation and LQCF from the first to N-th time instant are calculated as Equation (24) and Equation (25), respectively. By replacing **X** of Equation (25) with Equation (24), the LQCF, Equation (25), is obtained by Equation (26). In Equation (27), the bound on steering angle, $\delta_{\max}$, is imposed on the control input **U**. Moreover, instead of Equation (27), CTSAs can be imposed on the control input, as set in Equation (28). In Equation (28), $\mathbf{U}_f$ and $\mathbf{U}_r$ are the elements of **U** corresponding to δ_f and δ_r, respectively. β_0 and γ_0 are the values of β and γ, obtained from the current state $\mathbf{x}_0$. With this manner, the quadratic programming with the optimization variable **U**, the cost function J_{MPC}, and the bound constraints of Equation (27) and Equation (28) is formulated [7]. In this paper, the solver, quadprog(), provided in MATLAB R2019a optimization toolbox, was applied to find the optimum **U** at every time instant k. After finding the optimum, MPC usually selects the first element of the optimum **U** as the control input. In this paper, T_s and N are set to, respectively, 0.01 s and 30.

$$\mathbf{x}_{k+1} = \mathbf{F}\mathbf{x}_k + \mathbf{G}\mathbf{w}_k + \mathbf{H}\mathbf{u}_k \tag{19}$$

$$\mathbf{F} = \mathbf{I} + \mathbf{A} \cdot T_s, \ \mathbf{G} = \mathbf{B}_1 \cdot T_s, \ \mathbf{H} = \mathbf{B}_2 \cdot T_s \tag{20}$$

$$J_{MPC} = \sum_{k=0}^{N-1} \left(\mathbf{x}_k^T \mathbf{Q} \mathbf{x}_k + \mathbf{u}_k^T \mathbf{R} \mathbf{u}_k \right) \tag{21}$$

$$\mathbf{x}_{k+1} = \mathbf{F}^k \mathbf{x}_0 + \sum_{i=0}^{k-1} \mathbf{F}^{i-1} \mathbf{H} \mathbf{u}_{k-i-1} \tag{22}$$

$$\mathbf{X} = \begin{bmatrix} \mathbf{x}_1 \\ \mathbf{x}_2 \\ \mathbf{x}_3 \\ \vdots \\ \mathbf{x}_N \end{bmatrix}, \ \overline{\mathbf{F}} = \begin{bmatrix} \mathbf{F} \\ \mathbf{F}^2 \\ \mathbf{F}^3 \\ \vdots \\ \mathbf{F}^N \end{bmatrix}, \ \overline{\mathbf{H}} = \begin{bmatrix} \mathbf{H} & 0 & 0 & 0 & 0 \\ \mathbf{FH} & \mathbf{H} & 0 & 0 & 0 \\ \mathbf{F}^2\mathbf{H} & \mathbf{FH} & \mathbf{H} & 0 & 0 \\ \vdots & \vdots & \vdots & \ddots & 0 \\ \mathbf{F}^{N-1}\mathbf{H} & \mathbf{F}^{N-2}\mathbf{H} & \mathbf{F}^{N-3}\mathbf{H} & \cdots & \mathbf{H} \end{bmatrix}, \ \mathbf{U} = \begin{bmatrix} \mathbf{u}_0 \\ \mathbf{u}_1 \\ \mathbf{u}_2 \\ \vdots \\ \mathbf{u}_{N-1} \end{bmatrix} \tag{23}$$

$$\overline{\mathbf{Q}} = diag(\mathbf{Q}, \cdots, \mathbf{Q}), \ \overline{\mathbf{R}} = diag(\mathbf{R}, \cdots, \mathbf{R})$$

$$\mathbf{X} = \overline{\mathbf{F}}\mathbf{x}_0 + \overline{\mathbf{H}}\mathbf{U} \tag{24}$$

$$J_{MPC} = \mathbf{x}_0^T \mathbf{Q}\mathbf{x}_0 + \mathbf{X}^T \overline{\mathbf{Q}}\mathbf{X} + \mathbf{U}^T \overline{\mathbf{R}}\mathbf{U} \tag{25}$$

$$J_{MPC} = \mathbf{U}^T \left(\overline{\mathbf{H}}^T \overline{\mathbf{Q}}\overline{\mathbf{H}} + \overline{\mathbf{R}} \right) \mathbf{U} + 2\mathbf{x}_0^T \overline{\mathbf{F}}^T \overline{\mathbf{Q}}\overline{\mathbf{H}}\mathbf{U} \tag{26}$$

$$-\delta_{\max} \leq \mathbf{U} \leq \delta_{\max} \tag{27}$$

$$\begin{cases} -\alpha_m + \beta_0 + \dfrac{l_f \gamma_0}{v_x} \leq \mathbf{U}_f \leq \alpha_m + \beta_0 + \dfrac{l_f \gamma_0}{v_x} \\ -\alpha_m + \beta_0 - \dfrac{l_r \gamma_0}{v_x} \leq \mathbf{U}_r \leq \alpha_m + \beta_0 - \dfrac{l_r \gamma_0}{v_x} \end{cases} \tag{28}$$

Different from LQR, MPC can directly handle the constraints on the control inputs, i.e., δ_f and δ_r, as given in Equation (27) and Equation (28). However, MPC is to solve the optimization problem every time step, which requires a large amount of computations, compared to LQR with clipping. For the reason, there are hard limitations in implementing MPC on real vehicles. Let this denote MPC without and with the CTSA as MPCN and MPCC, respectively.

2.5. Control Allocation for LQR and MPC with IC#3

As shown in Equation (10), ΔM_z is calculated from *IC*#3. After the controllers calculate ΔM_z, it should be converted into the longitudinal forces applied to wheels. This force is generated by various combinations of the actuators, RWS, 4WIB, and 4WID. Typically, this conversion is accomplished with a process known as control allocation. In this paper, a weighted least square (WLS)-based method is employed for control allocation, which has been adopted in previous works [31,32].

Figure 4 illustrates the tire forces at each wheel and ΔM_z when ΔM_z is positive [25,30–32,35,39,40]. In Figure 4, four wheels are numbered as 1, 2, 3 and 4 in the order of the front left, front right, rear left and rear right wheels, respectively. In Figure 4, ΔF_{yr} represents F_y generated by the rear wheels through RWS. ΔF_{x1}, ΔF_{x2}, ΔF_{x3} and ΔF_{x4} denote F_x's generated by 4WID and 4WIB. If ΔF_{xi} is positive, it corresponds to T_{Di} generated by 4WID; otherwise, it corresponds to T_{Bi} generated by 4WIB. Those five tire forces need to be determined so as to generate ΔM_z. For the purpose, WLS-based method is selected as a control allocation method.
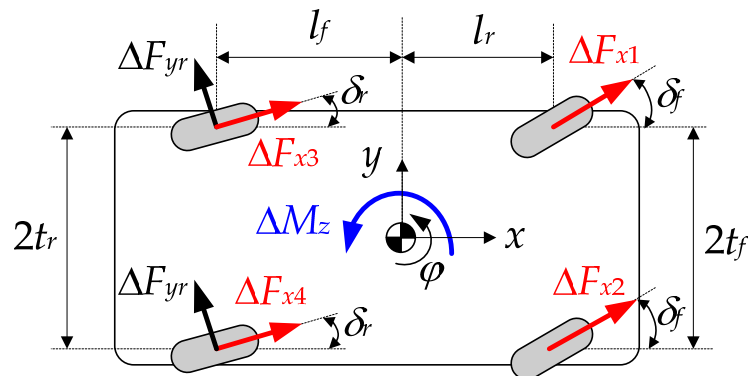

Figure 4. Geometric information and coordinate system of tire forces and ΔM_z.

The equilibrium condition among ΔM_z and tire forces is derived as Equation (29) from the geometric information depicted in Figure 4 [36,39,43,46]. The components of vector $\mathbf{z}$ are given in Equation (30).

$$\underbrace{\begin{bmatrix} z_1(t) & z_2(t) & z_3(t) & z_4(t) & z_5(t) \end{bmatrix}}_{\mathbf{z}(t)} \underbrace{\begin{bmatrix} \Delta F_{yr}(t) \\ \Delta F_{x1}(t) \\ \Delta F_{x2}(t) \\ \Delta F_{x3}(t) \\ \Delta F_{x4}(t) \end{bmatrix}}_{\mathbf{q}(t)} = \mathbf{z}(t)\mathbf{q}(t) = \Delta M_z(t) \tag{29}$$

$$\begin{cases} z_1(t) = 2l_r \cos \delta_r(t), \\ z_2(t) = -l_f \sin \delta_f(t) + t_f \cos \delta_f(t), \; z_3(t) = -l_f \sin \delta_f(t) - t_f \cos \delta_f(t), \\ z_4(t) = l_r \sin \delta_r(t) + t_r \cos \delta_r(t), \quad z_5(t) = l_r \sin \delta_r(t) - t_r \cos \delta_r(t) \end{cases} \tag{30}$$

The quadratic cost function for WLS is given as Equation (31). Within Equation (31), ζ_i is the product of μ and F_{zi} at the wheel i, i.e., μF_{zi}, which represents the friction circle radius. The vector of virtual weights, denoted as $\boldsymbol{\kappa}$, is introduced in Equation (31) for the purpose of selecting the combination of actuators [25,30–32,35,39]. The quadratic cost function, J_{EC} in Equation (32), is obtained from the constraint Equation (29). In previous research, the equilibrium condition Equation (29) should be satisfied for the purpose of generating ΔM_z. The cost functions, Equations (31) and (32), are summed into a single one (33) with the Lagrange multiplier, η. In Equation (33), it is important to set η to a value of 1 or higher; otherwise, the equilibrium condition Equation (29) will not be met. The optimal solution for Equation (33) is algebraically calculated as Equation (34) by taking the derivative of Equation (33) with respect to $\mathbf{q}$ [31,32].

$$\begin{cases} J_Q = \dfrac{\kappa_2 \Delta F_{x1}^2(t)}{\zeta_1^2} + \dfrac{\kappa_3 \Delta F_{x2}^2(t)}{\zeta_2^2} + \dfrac{\kappa_1 \Delta F_{yr}^2(t) + \kappa_4 \Delta F_{x3}^2(t)}{\zeta_3^2} + \dfrac{\kappa_1 \Delta F_{yr}^2(t) + \kappa_5 \Delta F_{x4}^2(t)}{\zeta_4^2} = \mathbf{q}^T(t)\Theta\mathbf{q}(t) \\ \Theta = \operatorname{diag}\left[\dfrac{1}{\zeta_3^2} + \dfrac{1}{\zeta_4^2}, \dfrac{1}{\zeta_1^2}, \dfrac{1}{\zeta_2^2}, \dfrac{1}{\zeta_3^2}, \dfrac{1}{\zeta_4^2} \right]\boldsymbol{\kappa} \\ \boldsymbol{\kappa} = \operatorname{diag}\begin{bmatrix} \kappa_1 & \kappa_2 & \kappa_3 & \kappa_4 & \kappa_5 \end{bmatrix} \end{cases} \tag{31}$$

$$J_{EC} = \{\mathbf{z}(t)\mathbf{q}(t) - \Delta M_z(t)\}^T \{\mathbf{z}(t)\mathbf{q}(t) - \Delta M_z(t)\} \tag{32}$$

$$J_{CA} = J_Q + \eta \cdot J_{EC} = \mathbf{q}^T(t)\Theta\mathbf{q}(t) + \eta\{\mathbf{z}(t)\mathbf{q}(t) - \Delta M_z(t)\}^T \{\mathbf{z}(t)\mathbf{q}(t) - \Delta M_z(t)\} \tag{33}$$

$$\mathbf{q}_{opt}(t) = \eta\left\{ \Theta + \eta\mathbf{z}^T(t)\mathbf{z}(t) \right\}^{-1} \mathbf{z}^T(t)\Delta M_z(t) \tag{34}$$

When WLS is applied to control allocation for *IC#3*, an arbitrary combination of actuators comprising RWS, 4WID, and 4WIB can be configured. To account for several actuator combinations, the virtual weights, denoted as κ_i, can be set to match a particular combination of those actuators [31,32]. The detailed usage of the virtual weights and the procedure to derive δ_r, T_{Di} and T_{Bi} of each wheel can be also found in the literature [31,32].

In the field of VSC or PTC, the friction circle constraint, as defined in Equation (35), has been included into the optimization procedure for control allocation [48–50]. This constraint can be transformed to define the tire force margin (TFM), as defined in Equation (36). TFM indicates how much extra tire force can be generated under VSC or PTC. If TFM is small, F_x and F_y are near its maximum, which indicates the fact that an extra actuator selected to generate these forces becomes useless. If TFM is zero, this indicates the fact that both F_x and F_y are saturated and that there are no margins to generate extra tire force for VSC or PTC. As shown in Equation (36), TFM becomes much smaller under low-friction road conditions. If CTSA is imposed, then it is expected that TFM easily becomes zero.

$$\{\mu F_z(t)\}^2 \geq F_x^2(t) + F_y^2(t) \tag{35}$$

$$\text{TFM}(t) = \mu F_z(t) - \sqrt{F_x^2(t) + F_y^2(t)} \tag{36}$$

3. Performance Measures for Path Tracking Control

In the domain of PTC, e_y and e_φ have been widely used as indicators for assessing path tracking performance. However, different from conventional PTC literature, this paper adopts a double lane change maneuver as the target path for collision avoidance [13,16,17,20,21,31,32]. This maneuver was employed to evaluate the reachability and agility of a path tracking controller [31,32]. Figure 5 shows both the target path and the trajectory of a vehicle. In Figure 5, the points A, B and C are on the target path, which represent the peak, zero-crossing and convergence points, respectively. The points D, E, F and G are on the vehicle trajectory, which represent the peak, zero-crossing, over-shoot and convergence points, respectively. Five metrics, M_X, M_Y, M_{OS}, M_{DX} and M_{SX}, representing path tracking performance, are defined as Equation (37), based on the points along the target path and vehicle trajectory in Figure 5. In Equation (37), the subscripts X and Y correspond to the x- and y-positions of the corresponding point, respectively.

$$\begin{cases} M_X = D_X - A_X = D_X - 73.20 \\ M_Y = D_Y - A_Y = D_Y - 3.53 \\ M_{DX} = E_X - B_X = E_X - 91.50 \\ M_{SX} = G_X - C_X = G_X - 190.00 \\ M_{OS} = \frac{|F_Y| - 1.65}{1.65 + 3.53} \times 100 \end{cases} \tag{37}$$
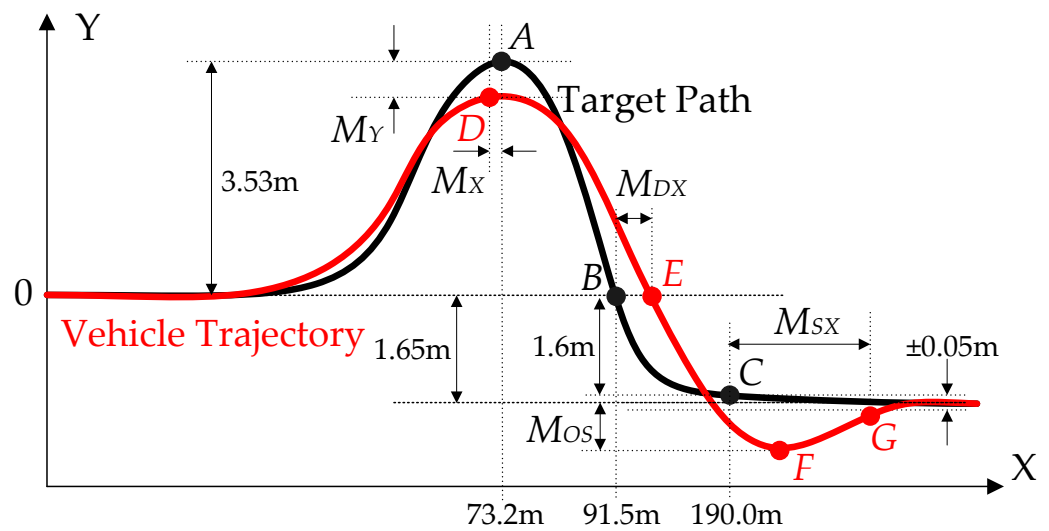

Figure 5. Measures used to tune PTC.

M_X and M_Y represent the peak's center and lateral offsets, respectively. In this study, agility and reachability are represented by M_X and M_Y, respectively. If M_Y exceeds -0.02 m, the controller's path tracking performance can be regarded as satisfactory. M_{OS} represents the percentage of overshoot, which is identical to that of automatic control theory. This indicates lateral damping, reflecting agility. In this paper, a satisfactory performance is achieved if M_{OS} remains below 16%, which is equivalent to an overshoot of 0.85 m. M_{DX} and M_{SX} represent the response delay and the settling delay, respectively. M_{DX} corresponds to a delay, standing for the agility of longitudinal motion. M_{DX} highly depends on μ. M_{SX} can be interpreted as the settling time, indicating the convergence speed of the vehicle's lateral motion toward a target y-position. M_{SX} is closely related to M_{OS}. In essence, smaller absolute values of these metrics correspond to improved path tracking performance.

As mentioned previously, VSC and LSC aim for yaw rate tracking and lateral stability, respectively. Typically, yaw rate tracking performance is assessed by the difference between real and reference yaw rates, while lateral stability performance is evaluated by the

magnitude of β. It has been considered satisfactory if β is less than 3 degrees [51]. Let the maximum absolute value of β be referred to as MASSA. The side-slip angular rate, when combined with β, has been also employed as a measure of lateral stability [30]. Let this denote the maximum absolute value of side-slip angular rate as MASSAR.

In this paper, the tuning parameters are the maximum allowable value ξ_i given in Equation (14) and the velocity gain k_v given in Equation (5). There are three tuning objectives when tuning these parameters in this paper. The first objective is collision avoidance, which is achieved by tuning parameters such that M_Y is larger than -0.02 m. Generally, the best M_{SX} is attained when M_{OS} is around 0.9, provided that M_Y exceeds -0.02 m. The second objective is path tracking, which is achieved by tuning parameters such that M_X, M_{DX} and M_{SX} are maintained as small as possible. Among them, the minimum of M_{DX} clearly depends on μ. The third objective is lateral stability, which is achieved by tuning parameters such that MASSA is less than $2°$.

4. Simulation and Discussion

To verify the effects of the CTSA on path tracking performance under low-friction road condition, a simulation was conducted. The path tracking controllers, LQRN, LQRC, MPCN and MPCC, were implemented with MATLAB/Simulink R2019a, connected to CarSim [52]. Test scenario was given in Figure 5. In the simulation, F-segment sedan model in CarSim was selected as a test vehicle [52]. From simulation with the model under step steering or steady-state cornering, the parameters and its values of the 2-DOF bicycle model were obtained as given in the reference [25,30–32]. In this paper, a first-order system was adopted to model actuators such as FWS and 4WS, and 4WIB and 4WID, where the bandwidths of these actuators are set to 5 Hz and 2 Hz, respectively. The initial v_x and μ were set to 60 km/h and 0.4, respectively. For the purpose of maintaining v_x as constant as possible, a built-in speed controller provided in CarSim was applied. The simulation horizon was set to 15 s.

Generally, the larger δ_r, the larger β. For the reason, it is necessary to limit ΔM_z to a certain value so as to make δ_r small for *IC*#3. $F_{y,max}$ from F-segment sedan model in CarSim is 7500 N where μ is 1 [52]. This will be 3000 N if μ is set to 0.4. As shown in Equation (29), F_y at front wheels, i.e., ΔF_{yf}, was not used to generate ΔM_z because δ_f is included in the control input. From the geometric information of the test vehicle, the maximum available yaw moment at rear wheels is calculated as $3000 \times 2 \times l_r = 11{,}400$ Nm. After ΔM_z was obtained from LQR with *IC*#3, it is limited by clipping it into 11,400 Nm in this paper. δ_{max} of front and rear wheels was set to $30°$. α_m was set to $5°$, which is referred from CarSim tire model as given in Figure 1.

The first simulation is done for LQRN and LQRC. Tables 2 and 3 show the simulation results of LQRN and LQRC. As mentioned earlier, the control parameters were tuned such that M_Y is larger than -0.02 m and M_{OS} is near 0.9. These two measures are nearly the same as shown in Tables 2 and 3. For the reason, these are not used for comparison. The percentages inside the parentheses in Table 3 represent the percentage reductions of M_X, M_{DX} and M_{SX} relative to the corresponding values given in Table 2 for each actuator combination. As shown in those tables, M_X, M_{DX} and M_{SX} of LQRC are improved, compared to those of LQRN. This indicates that the CTSA can effectively limit α to α_m, which generates $F_{y,max}$.

In case of LQRN, the actuator combination, FWS + 4WIB of *IC*#3, shows the best performance in terms of M_{DX} and M_{SX}. On the contrary, in case of LQRC, the actuator combination, FWS + RWS of *IC*#3, shows the best performance in terms of M_X, M_{DX} and M_{SX}. Moreover, this combination is superior to *IC*#2 of LQRC, which used the identical actuators, FWS and RWS. This means that any actuator combinations using 4WID and 4WIB are inferior to FWS + RWS of *IC*#3. The input configurations, *IC*#1 and *IC*#2, of LQR do not require a control allocation. In *IC*#1 and *IC*#2, δ_f and δ_r, are directly computed and applied into steering actuators. However, *IC*#3 of LQR requires a control allocation, which is complex and time-consuming. Due to its simplicity, *IC*#1 and *IC*#2 of LQR are

recommended if one do not think the difference between *IC*#1/*IC*#2 and *IC*#3 is significant. From these results, it can be concluded that CTSA is strongly recommended for better path tracking. Moreover, it is also concluded that FWS + RWS of *IC*#3 is recommended as an actuator combination instead of *IC*#2 in terms of path tracking performance, and that *IC*#1 or *IC*#2 is recommended as an input configuration instead of *IC*#3 in terms of simplicity and ease of implementation.

Table 2. Summary of the simulation results with LQRN for *IC*#1, *IC*#2, *IC*#3.

	Actuator Combinations	M_X (m)	M_Y (m)	M_{OS}	M_{DX} (m)	M_{SX} (m)	MASSA (deg)	MASSAR (deg/s)
IC#1	FWS	1.25	−0.018	1.0	8.58	4.39	0.58	13.19
IC#2	4WS	1.58	−0.017	0.9	8.94	4.97	1.26	13.99
IC#3 FWS	+RWS	1.15	−0.019	0.9	8.51	4.31	0.79	13.16
	+RWS + 4WID	1.24	−0.018	0.9	8.47	4.54	0.77	13.13
	+RWS + 4WIB	1.62	−0.018	0.9	8.66	4.11	0.80	12.97
	+RWS + 4WID + 4WIB	1.47	−0.018	0.9	9.44	5.52	0.80	13.25
	+4WID	1.67	−0.018	0.9	9.04	5.10	0.60	13.38
	+4WIB	1.69	−0.017	0.9	8.14	3.57	0.68	12.71
	+4WID + 4WIB	1.66	−0.017	0.9	9.64	5.71	0.63	13.47

Table 3. Summary of the simulation results with LQRC for *IC*#1, *IC*#2, *IC*#3.

	Actuator Combinations	M_X (m)	M_Y (m)	M_{OS}	M_{DX} (m)	M_{SX} (m)	MASSA (deg)	MASSAR (deg/s)
IC#1	FWS	0.77 (38%)	−0.017	0.9	5.95 (31%)	1.67 (62%)	0.87	13.14
IC#2	4WS	1.01 (36%)	−0.017	0.9	6.03 (33%)	1.42 (71%)	0.70	12.90
IC#3 FWS	+RWS	0.29 (75%)	−0.017	0.9	5.28 (38%)	0.28 (94%)	0.83	13.73
	+RWS + 4WID	0.36 (71%)	−0.018	0.9	5.78 (32%)	1.24 (73%)	0.79	13.52
	+RWS + 4WIB	1.07 (34%)	−0.018	0.9	6.36 (27%)	1.71 (58%)	0.91	13.76
	+RWS + 4WID + 4WIB	0.46 (69%)	−0.018	0.9	5.57 (41%)	0.50 (91%)	0.87	14.48
	+4WID	1.13 (32%)	−0.018	0.9	7.63 (16%)	4.30 (16%)	0.96	13.36
	+4WIB	1.44 (15%)	−0.018	0.9	7.38 (9%)	3.50 (2%)	1.63	13.61
	+4WID + 4WIB	0.99 (40%)	−0.018	0.9	6.16 (36%)	1.40 (76%)	0.83	13.23

Figure 6 shows the plots drawn from the simulation results of *IC*#1 of LQRN and LQRC. In Figure 6d,e, the legends, FL, FR, RL and RR, stand for front left, front right, rear left and rear right wheels, respectively. As shown in Figure 6a, δ_f was limited to a certain value near α_m. Compared to the limits on the steering angles, ±30°, α_m, i.e., 5°, is quite small. As a result, F_y's at front wheels were not saturated and were generated to its own maximum, as shown in Figure 6d. For the reason, TFMs of front wheels become 0, as shown in Figure 6e, and the path tracking performance of LQRC was improved, compared to LQRN, as shown in Figure 6b. Because the maximum F_y's are generated by FWS with CTSA of LQRC, TFMs of LQRC at front wheels became zero, which indicates the other actuators are not needed for FWS to generate extra F_y's. This can be checked in Figure 6e. On the other hand, as shown in Figure 6d, TFMs of LQRN at front wheels did not become zero, which means the other actuators can generate extra F_y's at front wheels.

The second simulation is done for MPCN and MPCC. Tables 4 and 5 show the simulation results of MPCN and MPCC. As shown in those tables, M_X, M_{DX} and M_{SX} of MPCC

are improved, compared to those of MPCN. This coincides with the results of LQRC. This means that CTSA can effectively limit α to α_m, which cause the maximum F_y.
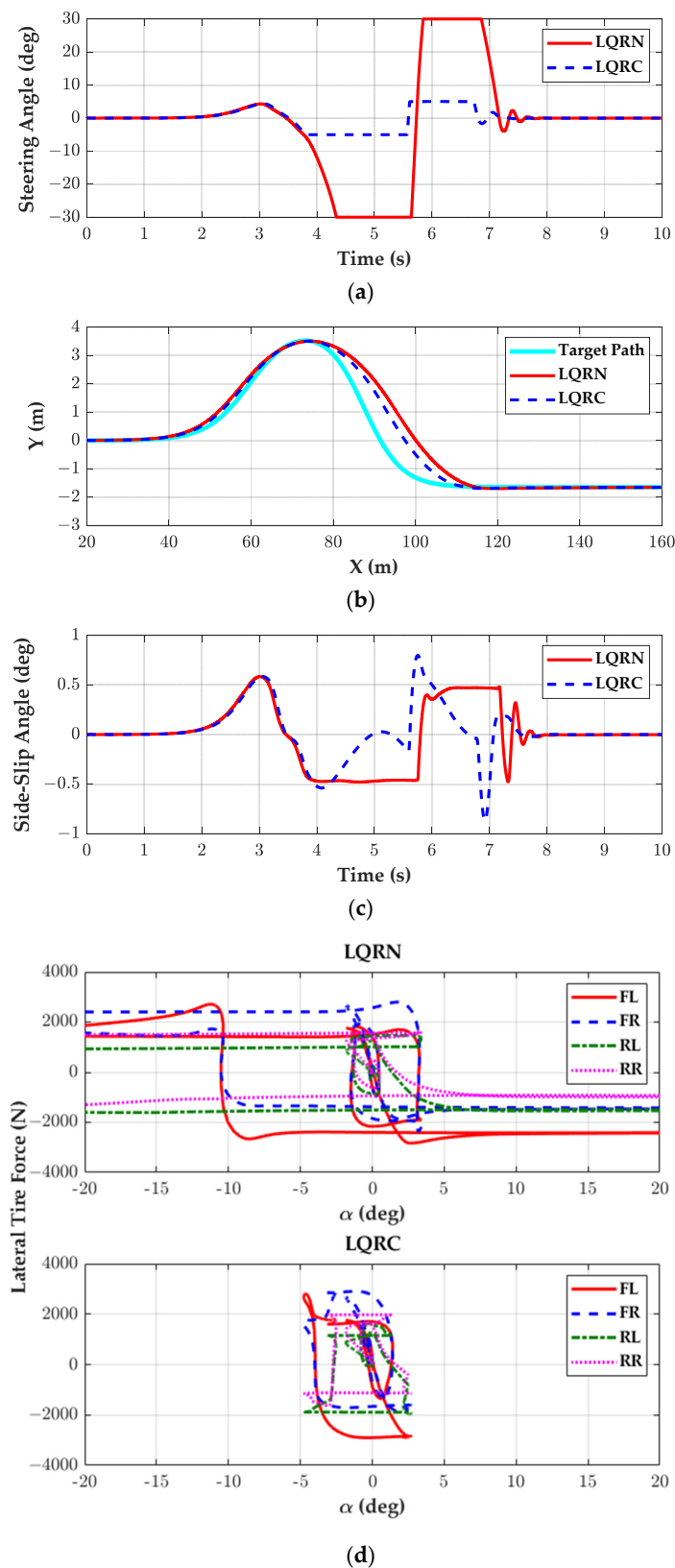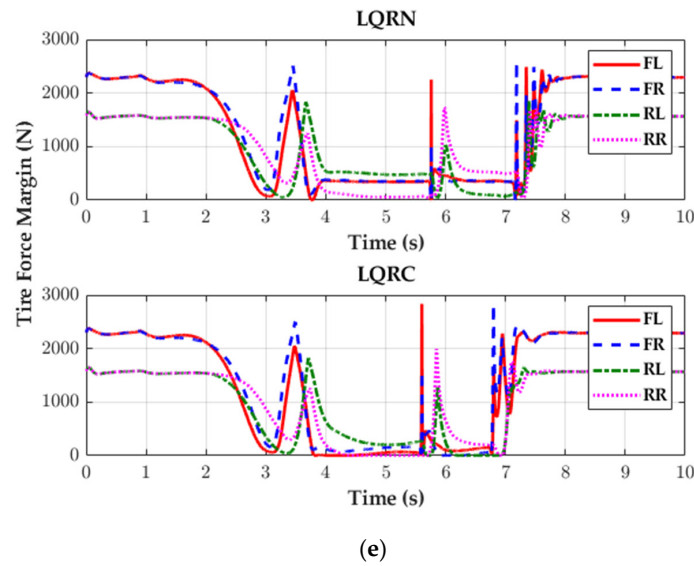

Figure 6. *Cont.*

(**e**)

Figure 6. Simulation results with *IC#1* of LQRN and LQRC. (**a**) Steering angles; (**b**) Trajectories; (**c**) Side-slip angles; (**d**) slip angles vs. lateral tire forces; (**e**) Tire force margin.

Table 4. Summary of the simulation results with MPCN for *IC#1*, *IC#2*, *IC#3*.

	Actuator Combinations	M_X (m)	M_Y (m)	M_{OS}	M_{DX} (m)	M_{SX} (m)	MASSA (deg)	MASSAR (deg/s)
IC#1	FWS	2.10	−0.018	0.9	9.42	5.67	0.57	12.92
IC#2	4WS	2.17	−0.019	0.9	9.42	5.95	1.48	13.32
IC#3 FWS	+RWS	2.07	−0.018	0.9	9.44	5.36	0.78	13.23
	+RWS + 4WID	2.45	−0.018	0.9	9.78	5.84	0.80	13.25
	+RWS + 4WIB	2.35	−0.019	0.9	9.42	4.85	0.86	12.82
	+RWS + 4WID + 4WIB	2.17	−0.019	0.9	10.16	6.34	0.83	13.01
	+4WID	2.35	−0.019	0.9	9.80	5.83	0.61	13.38
	+4WIB	2.05	−0.019	0.9	8.25	3.77	0.66	11.77
	+4WID + 4WIB	2.17	−0.019	0.9	10.16	6.34	0.83	13.01

Table 5. Summary of the simulation results with MPCC for *IC#1*, *IC#2*, *IC#3*.

|	Actuator Combinations	M_X (m)	M_Y (m)	M_{OS}	M_{DX} (m)	M_{SX} (m)	MASSA (deg)	MASSAR (deg/s)
IC#1	FWS	1.54 (27%)	−0.018	0.9	6.72 (29%)	2.69 (53%)	0.83	12.83
IC#2	4WS	1.54 (29%)	−0.019	0.9	6.68 (29%)	2.49 (58%)	1.33	13.45
IC#3 FWS	+RWS	1.22 (41%)	−0.018	0.9	6.20 (34%)	1.32 (75%)	0.83	13.84
	+RWS + 4WID	1.45 (41%)	−0.018	0.9	7.12 (27%)	2.88 (51%)	0.80	13.15
	+RWS + 4WIB	1.85 (21%)	−0.018	0.9	6.87 (27%)	2.63 (46%)	0.84	12.57
	+RWS + 4WID + 4WIB	1.41 (35%)	−0.019	0.9	6.47 (36%)	1.57 (75%)	0.84	13.73
	+4WID	1.85 (21%)	−0.019	0.9	8.53 (13%)	5.33 (9%)	0.90	13.26
	+4WIB	2.08 (2%)	−0.018	0.9	7.73 (6%)	3.40 (10%)	1.88	11.31
	+4WID + 4WIB	1.41 (35%)	−0.019	0.9	6.47 (36%)	1.57 (75%)	0.84	13.73

Figure 7 show the plots drawn from the simulation results of *IC*#1 of MPCN and MPCC. In Figure 7d,e, the legends, FL, FR, RL and RR, stand for front left, front right, rear left and rear right wheels, respectively. As shown in Figure 7c, F_y's of MPCN were saturated due to the large α. On the contrary, F_y's of MPCC were not saturated due to the CTSA, as shown in Figure 7c. Because the maximum F_y's are generated by FWS with the CTSA of MPCC, TFM of MPCC at front wheels became zero, which means the other actuators are not needed for FWS to generate extra F_y's. This can be checked in Figure 7d. On the other hand, as shown in Figure 6d, TFM of MPCN at front wheels did not become zero, which means the other actuators can generate extra F_y's at front wheels.
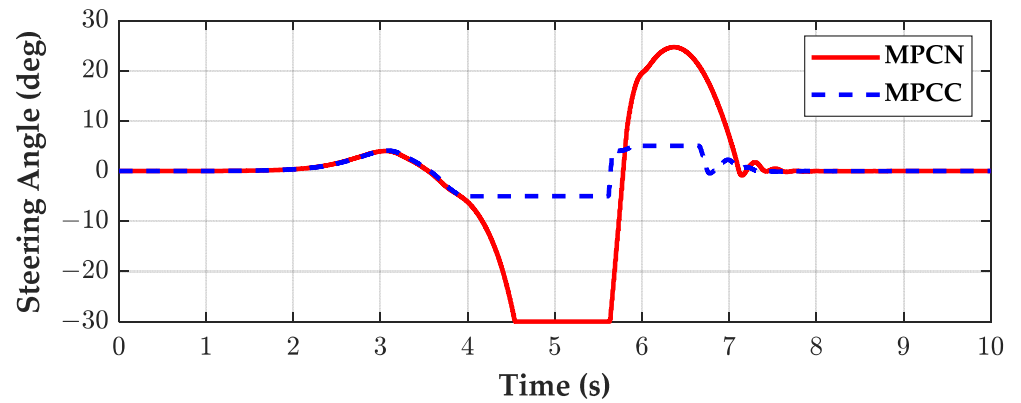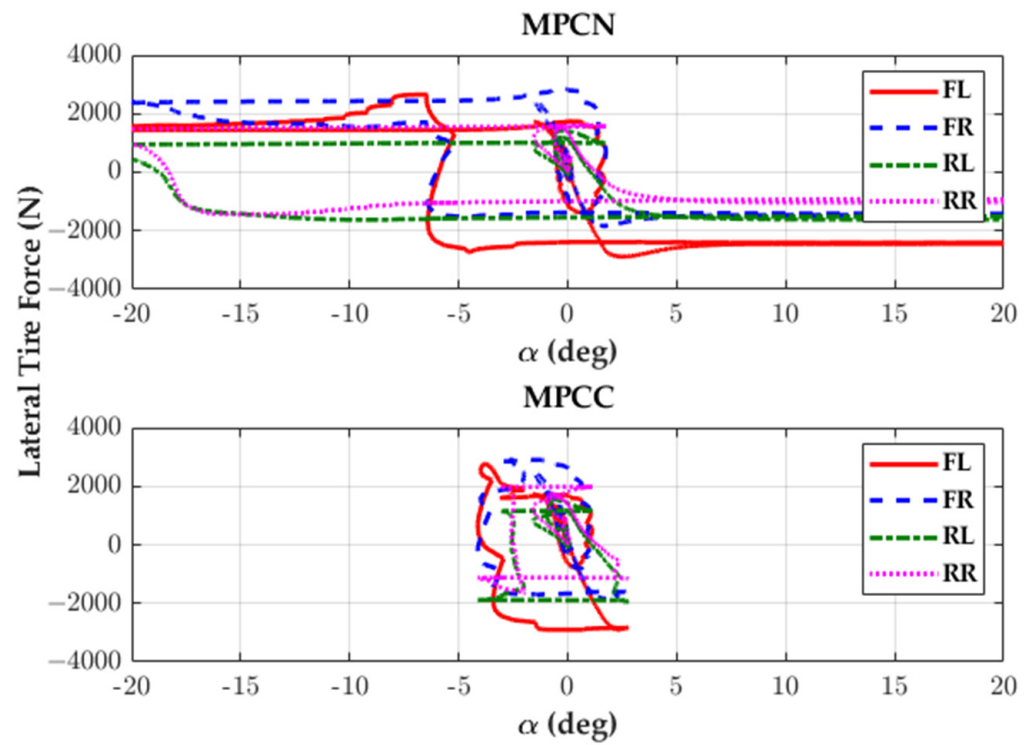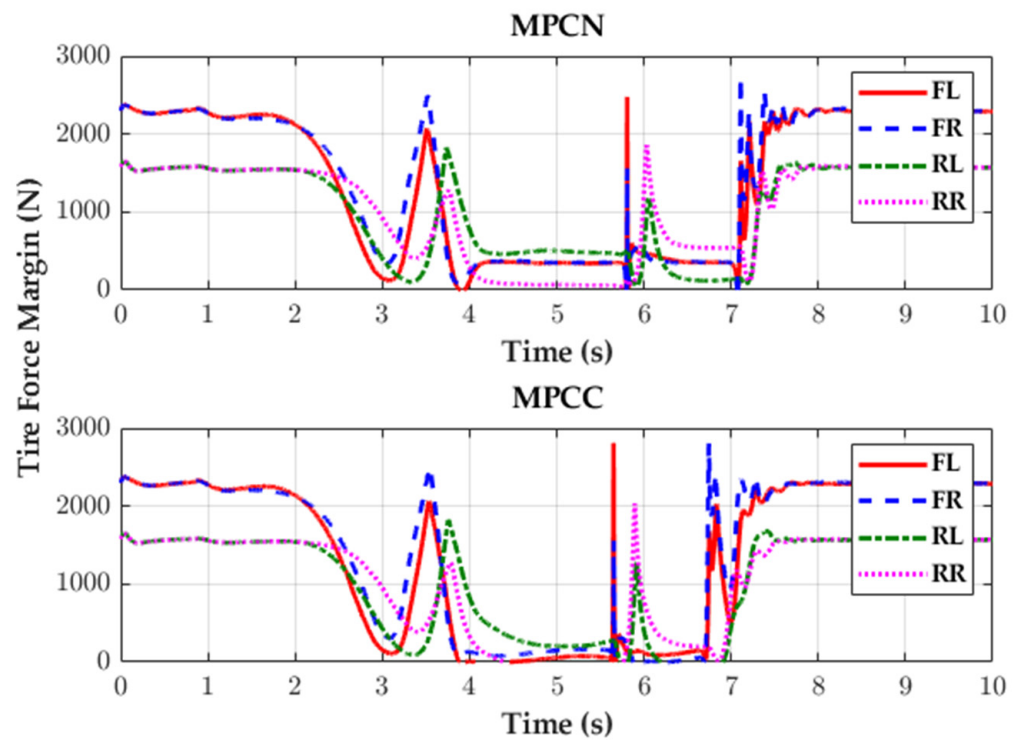

(a)
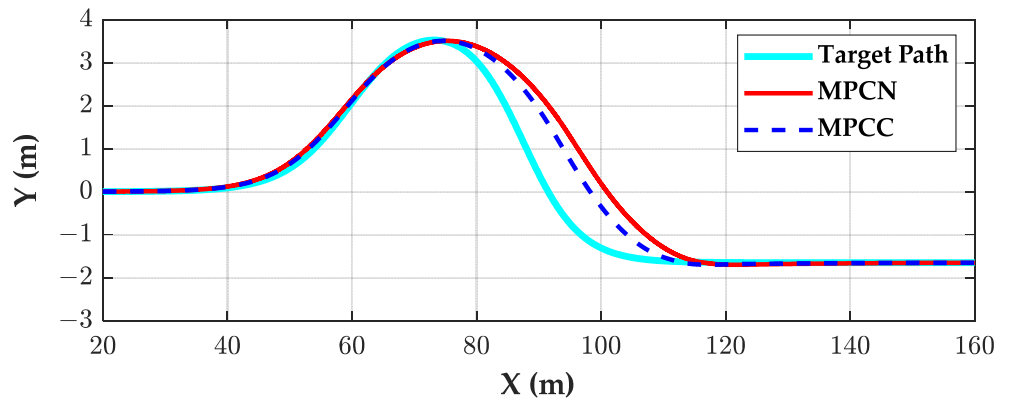
(b)
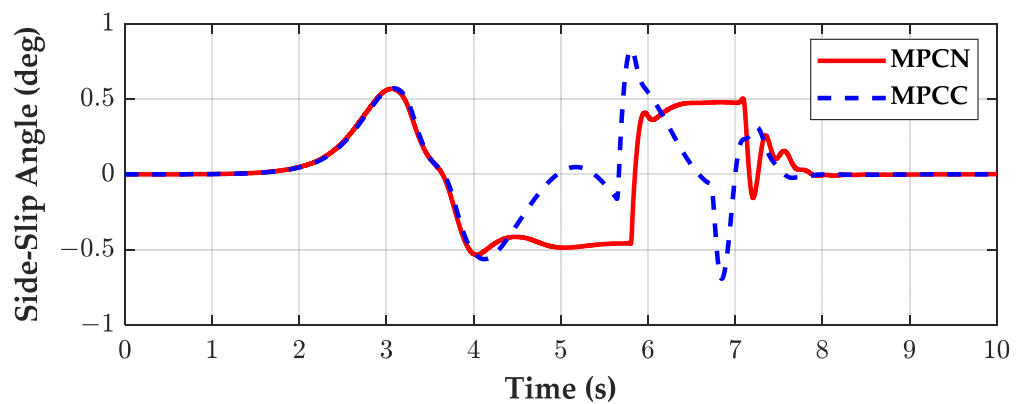
(c)

Figure 7. *Cont.*

(**d**)

(**e**)

Figure 7. Simulation results with *IC*#1 of MPCN and MPCC. (**a**) Steering angles; (**b**) Trajectories; (**c**) Side-slip angles; (**d**) slip angles vs. lateral tire forces; (**e**) Tire force margin.

5. Conclusions

This paper presented a path tracking controller with CTSA on low-friction road surface. The contents of this paper are summarized as follows:

- This paper presented a method to impose a CTSA such that the maximum lateral force is generated on low-friction road surface. The constraint is derived simply from the definition of tire slip angle and easily applied into LQR and MPC. From simulation results, the CTSA can greatly improve the path tracking performance on low-friction surface.

- The proposed CTSA makes the most of the lateral tire force. This means that there are little tire forces left to improve the control performance. Under that condition, it was shown that various combinations composed from RWS, 4WID, and 4WIB have little effects on control performance.

- From the simulation results, it is recommended that LQR is better than MPC in terms of computation time and simplicity of controller structure. Moreover, RWS calculated from the control yaw moment in *IC*#3 provided the best path tracking result. However, *IC*#3 requires a control allocation, which is complex and time-consuming, compared to *IC*#1 and *IC*#2. For the reason, *IC*#1 and *IC*#2 are preferred to *IC*#3 due to its simplicity and ease of implementation if one do not think the difference between *IC*#1/*IC*#2 and *IC*#3 is significant.

The CTSA adopted in this paper are easy to derive and simple to apply to LQR or MPC. Moreover, a procedure to design LQR with bound constraints on the control inputs are not needed. For the reason, it is recommended that a path tracking controller should include the CTSA.

The limitations of the proposed method are to measure the yaw rate and velocities and to estimate the side-slip angle with available sensors. To overcome these issues, sensor specification and estimation schemes are to be investigated. In further research, experiments on a scaled vehicle will be done with the proposed method. Moreover, extra experiments will be performed on real vehicles on low friction conditions.

Author Contributions: J.L. conceptualized the main idea, and designed this study. S.Y. supported fund for this study. S.Y. participated in formulating the idea, as well as validating the proposed method and results. S.Y. implemented the methodology and obtained results. J.L. and S.Y. analyzed the results and drafted the manuscript. All authors have read and agreed to the published version of the manuscript.

Institutional Review Board Statement: Not applicable.

Informed Consent Statement: Not applicable.

Data Availability Statement: The data presented in this study are available in the references [31,32].

Conflicts of Interest: The authors declare no conflicts of interest.

Nomenclature

4WS	4-wheel steering
4WIB	4-wheel independent braking
4WID	4-wheel independent drive
CTSA	constraint on tire slip angle
FWS	front wheel steering
LQCF	LQ cost function
LQR	linear quadratic regulator
LQRC	LQR with CTSAs
LQRN	LQR without CTSAs
LSC	lateral stability control

MASSA	maximum absolute value of the side-slip angle over simulation horizon
MASSAR	maximum absolute value of side-slip angular rate over simulation horizon
MPC	model predictive control
MPCC	MPC with CTSAs
MPCN	MPC without CTSAs
RWS	rear wheel steering
SMC	sliding mode control
TFM	tire force margin derived from the friction circle (N)
VSC	vehicle stability control
WLS	weighted least square
C_f, C_r	cornering stiffness of front and rear tires (N/rad)
e_y, e_φ	lateral offset error (m) and heading error (rad)
F_x, F_y, F_z	longitudinal, lateral and vertical tire forces of a tire (N)
F_{xi}, F_{yi}, F_{zi}	longitudinal, lateral and vertical tire forces of i-th wheel (N)
F_{yf}, F_{yr}	front and rear lateral tire forces in the 2-DOF bicycle model (N)
$F_{y,max}$	maximum lateral tire force of a tire at $\alpha = \alpha_m$ (N)
$\mathbf{z}$	matrix used for the constraint on RWS and 4WS in WLS based method
I_z	yaw moment of inertial (kg·m^2)
J_i	LQ cost function for the input configuration *IC#i*
$\mathbf{K}_{LQR,i}$	gain matrix of LQR for input configuration *IC#i*
k_v	velocity gain for preview distance (s^{-1})
L_p	preview distance (m)
l_f, l_r	distance from a center of gravity to front and rear axles (m)
M_X, M_Y	differences between x- and y-positions at the peak points of the target path (m)
M_{DX}, M_{SX}	response and settling delays of vehicle trajectory with respect to target path (m)
M_{OS}	percentage overshoot along y-direction in the lower lane of the target path
N	prediction horizon of MPC
m	vehicle total mass (kg)
$\mathbf{q}$	vector of tire forces as a solution of WLS based method
T_{Bi}, T_{Di}	braking and traction torques generated at i-th wheel from ΔM_z (N·m)
T_s	sampling interval of discrete-time system (s)
t_f, t_r	half of track widths of front and rear axles (m)
v_x, v_y	longitudinal and lateral velocities of CoG of a vehicle (m/s)
α	tire slip angle (rad)
α_m	tire slip angle where the maximum lateral tire force comes out (rad)
α_f, α_r	tire slip angles of front and rear wheels (rad)
β	side-slip angle of CoG of a vehicle (rad) = $\tan^{-1}(v_y/v_x) \approx (v_y/v_x)$
δ_f, δ_r	front and rear steering angles as a control input in LQR and MPC (rad)
ΔF_{yr}	control lateral tire force of rear wheels generated by an actuator (N)
ΔF_{xi}	control longitudinal tire force at i-th wheel, generated by an actuator (N)
ΔM_z	control yaw moment as a control input in LQR and MPC (N·m)
η	tuning parameter on relaxation term of equality constraint
γ, γ_d	real and reference yaw rates (rad/s)
χ	curvature at a particular point on a target path (m^{-1})
κ_i	virtual weight on the longitudinal and lateral tire forces
$\boldsymbol{\kappa}$	the vector of virtual weights
ξ_i	the maximum allowable value of i-th term in LQ cost function
φ	heading angle of a vehicle (rad)
φ_d	desired heading angle obtained at preview point (rad)
μ	tire-road friction coefficient
ρ_i	weight on i-th term in LQCF
Θ	weighting matrix of WLS based method
ζ	the product of μ and $F_z = \mu F_z$

References

1. Montanaro, U.; Dixit, S.; Fallaha, S.; Dianatib, M.; Stevensc, A.; Oxtobyd, D.; Mouzakitisd, A. Towards connected autonomous driving: Review of use-cases. *Veh. Syst. Dyn.* **2019**, *57*, 779–814. [CrossRef]
2. Yurtsever, E.; Lambert, J.; Carballo, A.; Takeda, K. A survey of autonomous driving: Common practices and emerging technologies. *IEEE Access* **2020**, *8*, 58443–58469. [CrossRef]
3. Omeiza, D.; Webb, H.; Jirotka, M.; Kunze, M. Explanations in autonomous driving: A survey. *IEEE Trans. Intell. Transp. Syst.* **2022**, *23*, 10142–10162. [CrossRef]
4. Paden, B.; Cap, M.; Yong, S.Z.; Yershov, D.; Frazzoli, E. A survey of motion planning and control techniques for self-driving urban vehicles. *IEEE Trans. Intell. Veh.* **2016**, *1*, 33–55. [CrossRef]
5. Sorniotti, A.; Barber, P.; De Pinto, S. Path tracking for automated driving: A tutorial on control system formulations and ongoing research. In *Automated Driving*; Watzenig, D., Horn, M., Eds.; Springer: Cham, Switzerland, 2017.
6. Amer, N.H.; Hudha, H.Z.K.; Kadir, Z.A. Modelling and control strategies in path tracking control for autonomous ground vehicles: A review of state of the art and challenges. *J. Intell. Robot. Syst.* **2017**, *86*, 225–254. [CrossRef]
7. Bai, G.; Meng, Y.; Liu, L.; Luo, W.; Gu, Q.; Liu, L. Review and comparison of path tracking based on model predictive control. *Electronics* **2019**, *8*, 1077. [CrossRef]
8. Yao, Q.; Tian, Y.; Wang, Q.; Wang, S. Control strategies on path tracking for autonomous vehicle: State of the art and future challenges. *IEEE Access* **2020**, *8*, 161211–161222. [CrossRef]
9. Rokonuzzaman, M.; Mohajer, N.; Nahavandi, S.; Mohamed, S. Review and performance evaluation of path tracking controllers of autonomous vehicles. *IET Intell. Transp. Syst.* **2021**, *15*, 646–670. [CrossRef]
10. Stano, P.; Montanaro, U.; Tavernini, D.; Tufo, M.; Fiengo, G.; Novella, L.; Sorniotti, A. Model predictive path tracking control for automated road vehicles: A review. *Annu. Rev. Control* **2022**, *55*, 194–236. [CrossRef]
11. Ren, Y.; Zheng, L.; Khajepour, A. Integrated model predictive and torque vectoring control for path tracking of 4-wheeldriven autonomous vehicles. *IET Intell. Transp. Syst.* **2019**, *13*, 98–107. [CrossRef]
12. Zhang, B.; Zong, C.; Chen, G.; Li, G. An adaptive-prediction-horizon model prediction control for path tracking in a four-wheel independent control electric vehicle. *Proc. Inst. Mech. Eng. Part D J. Automob. Eng.* **2019**, *233*, 3246–3262. [CrossRef]
13. Chen, X.; Peng, Y.; Hang, P.; Tang, T. Path tracking control of four-wheel independent steering electric vehicles based on optimal control. In Proceedings of the 2020 39th Chinese Control Conference (CCC), Shenyang, China, 27–30 July 2020; pp. 5436–5442.
14. Guo, L.; Ge, P.; Yue, M.; Li, J. Trajectory tracking algorithm in a hierarchical strategy for electric vehicle driven by four independent in-wheel motors. *J. Chin. Inst. Eng.* **2020**, *43*, 807–818. [CrossRef]
15. He, Z.; Nie, L.; Yin, Z.; Huang, S. A two-layer controller for lateral path tracking control of autonomous vehicles. *Sensors* **2020**, *20*, 3689. [CrossRef] [PubMed]
16. Wu, H.; Si, Z.; Li, Z. Trajectory tracking control for four-wheel independent drive intelligent vehicle based on model predictive control. *IEEE Access* **2020**, *8*, 73071–73081. [CrossRef]
17. Wu, H.; Li, Z.; Si, Z. Trajectory tracking control for four-wheel independent drive intelligent vehicle based on model predictive control and sliding mode control. *Adv. Mech. Eng.* **2021**, *13*, 9. [CrossRef]
18. Hang, P.; Chen, X. Path tracking control of 4-wheel steering autonomous ground vehicles based on linear parameter-varying system with experimental verification. *Proc. Inst. Mech. Eng. Part I J. Syst. Control Eng.* **2021**, *235*, 411–423. [CrossRef]
19. Xie, J.; Xu, X.; Wang, F.; Tang, Z.; Chen, L. Coordinated control based path following of distributed drive autonomous electric vehicles with yaw-moment control. *Cont. Eng. Prac.* **2021**, *106*, 104659. [CrossRef]
20. Xiang, C.; Peng, H.; Wang, W.; Li, L.; An, Q.; Cheng, S. Path tracking coordinated control strategy for autonomous four in-wheel-motor independent-drive vehicles with consideration of lateral stability. *Proc. Inst. Mech. Eng. Part D J. Automob. Eng.* **2021**, *235*, 1023–1036. [CrossRef]
21. Yang, K.; Tang, X.; Qin, Y.; Huang, Y.; Wang, H.; Pu, H. Comparative study of trajectory tracking control for automated vehicles via model predictive control and robust H-infinity state feedback control. *Chin. J. Mech. Eng.* **2021**, *34*, 74. [CrossRef]
22. Wang, G.; Liu, L.; Meng, Y.; Gu, Q.; Bai, G. Integrated path tracking control of steering and braking based on holistic MPC. *IFAC PapersOnLine* **2021**, *54*, 45–50. [CrossRef]
23. Tong, Y.; Jing, H.; Kuang, B.; Wang, G.; Liu, F.; Yang, Z. Trajectory tracking control for four-wheel independently driven electric vehicle based on model predictive control and sliding model control. In Proceedings of the 2021 5th CAA International Conference on Vehicular Control and Intelligence (CVCI), Tianjin, China, 29–31 October 2021.
24. Sun, X.; Wang, Y.; Hu, W.; Cai, Y.; Huang, C.; Chen, L. Path tracking control strategy for the intelligent vehicle considering tire nonlinear cornering characteristics in the PWA form. *J. Frankl. Inst.* **2022**, *359*, 2487–2513. [CrossRef]
25. Jeong, Y.; Yim, S. Integrated path tracking and lateral stability control with four-wheel independent steering for autonomous electric vehicles on low-friction roads. *Machines* **2022**, *10*, 650. [CrossRef]
26. Hu, H.; Bei, S.; Zhao, Q.; Han, X.; Zhou, D.; Zhou, X.; Li, B. Research on trajectory tracking of sliding mode control based on adaptive preview time. *Actuators* **2022**, *11*, 34. [CrossRef]
27. Barari, A.; Afshari, S.S.; Liang, X. Coordinated control for path-following of an autonomous four in-wheel motor drive electric vehicle. *Proc. Inst. Mech. Eng. Part C J. Mech. Eng. Sci.* **2022**, *236*, 6335–6346. [CrossRef] [PubMed]
28. Wang, G.; Liu, L.; Meng, Y.; Gu, Q.; Bai, G. Integrated path tracking control of steering and differential braking based on tire force distribution. *Int. J. Control Autom. Syst.* **2022**, *20*, 536–550. [CrossRef]

29. Wang, W.; Zhang, Y.; Yang, C.; Qie, T.; Ma, M. Adaptive model predictive control-based path following control for four-wheel independent drive automated vehicles. *IEEE Trans. Intell. Transp. Syst.* **2022**, *23*, 14399–14412. [CrossRef]

30. Lee, J.; Yim, S. Comparative study of path tracking controllers on low-friction roads for autonomous vehicles. *Machines* **2023**, *11*, 403. [CrossRef]

31. Park, M.; Yim, S. Comparative study on effects of input configurations of linear quadratic controller on path tracking performance under low-friction condition. *Actuators* **2023**, *12*, 153. [CrossRef]

32. Park, M.; Yim, S. Comparative study on coordinated control of path tracking and vehicle stability for autonomous vehicles on low-friction roads. *Actuators* **2023**, *12*, 398. [CrossRef]

33. Wong, H.Y. *Theory of Ground Vehicles*, 3rd ed.; John Wiley and Sons, Inc.: New York, NY, USA, 2001.

34. Rajamani, R. *Vehicle Dynamics and Control*; Springer: New York, NY, USA, 2006.

35. Nah, J.; Yim, S. Vehicle stability control with four-wheel independent braking, drive and steering on in-wheel motor-driven electric vehicles. *Electronics* **2020**, *9*, 1934. [CrossRef]

36. Ahangarnejad, A.H.; Radmehr, A.; Ahmadian, M. A review of vehicle active safety control methods: From antilock brakes to semiautonomy. *J. Vib. Control* **2021**, *27*, 1683–1712. [CrossRef]

37. Katsuyama, E.; Yamakado, M.; Abe, M. A state-of-the art review: Toward a novel vehicle dynamics control concept taking the driveline of electric vehicles into account as promising control actuators. *Veh. Syst. Dyn.* **2021**, *59*, 976–1025. [CrossRef]

38. Peng, H.; Chen, X. Active safety control of X-by-wire electric vehicles: A survey. *SAE Int. J. Veh. Dyn. Stab. NVH* **2022**, *6*, 115–133. [CrossRef]

39. Yim, S.; Kim, S.; Yun, H. Coordinated control with electronic stability control and active front steering using the optimum yaw moment distribution under a lateral force constraint on the active front steering. *Proc. Inst. Mech. Eng. Part D J. Automob. Eng.* **2016**, *230*, 581–592. [CrossRef]

40. Nah, J.; Yim, S. Vehicle dynamic control with 4WS, ESC and TVD under constraint on front slip angles. *Energies* **2021**, *14*, 6306. [CrossRef]

41. Park, G.; Han, K.; Nam, K.; Kim, H.; Choi, S.B. Torque vectoring algorithm of electronic-four-wheel drive vehicles for enhancement of cornering performance. *IEEE Trans. Veh. Technol.* **2020**, *69*, 3668–3679. [CrossRef]

42. Heo, H.; Joa, E.; Yi, K.; Kim, K. Integrated chassis control for enhancement of high speed cornering performance. *SAE Int. J. Commer. Veh.* **2015**, *8*, 102–109. [CrossRef]

43. Her, H.; Joa, E.; Yi, K.; Kim, K. Integrated chassis control for optimized tyre force coordination to enhance the limit handling performance. *Proc. Inst. Mech. Eng. Part D J. Automob. Eng.* **2016**, *230*, 1011–1026. [CrossRef]

44. Her, H.; Koh, Y.; Joa, E.; Yi, K.; Kim, K. An integrated control of differential braking, front/rear traction, and active roll moment for limit handling performance. *IEEE Trans. Veh. Technol.* **2016**, *65*, 4288–4300. [CrossRef]

45. Joa, E.; Yi, K.; Sohn, K.; Bae, H. Four-wheel independent brake control to limit tire slip under unknown road conditions. *Cont. Eng. Prac.* **2018**, *76*, 79–95. [CrossRef]

46. Bryson, A.E.; Ho, Y.C. *Applied Optimal Control*; Hemisphere: New York, NY, USA, 1975.

47. Kim, H.H.; Ryu, J. Sideslip angle estimation considering short-duration longitudinal velocity variation. *Int. J. Automot. Technol.* **2011**, *12*, 545–553. [CrossRef]

48. de Castro, R.; Tanelli, M.; Araújo, R.E.; Savaresi, S.M. Design of safety-oriented control allocation strategies for overactuated electric vehicles. *Veh. Syst. Dyn.* **2014**, *52*, 1017–1046. [CrossRef]

49. Rezaeian, A.; Zarringhalam, R.; Fallah, S.; Melek, W.; Khajepour, A.; Chen, S.-K.; Moshchuck, N.; Litkouhi, B. Novel tire force estimation strategy for real-time implementation on vehicle applications. *IEEE Trans. Veh. Technol.* **2015**, *64*, 2231–2241. [CrossRef]

50. Wang, J.; Wang, R.; Jing, H.; Chen, N. Coordinated active steering and four-wheel independent driving/braking control with control allocation. *Asian J. Control* **2016**, *18*, 98–111. [CrossRef]

51. National Highway Traffic Safety Administration. *FMVSS No. 126, Electronic Stability Control Systems: NHTSA Final Regulatory Impact Analysis*; National Highway Traffic Safety Administration: Washington, DC, USA, 2007.

52. Mechanical Simulation Corporation. *VS Browser: Reference Manual, the Graphical User Interfaces of BikeSim, CarSim, and TruckSim*; Mechanical Simulation Corporation: Ann Arbor, MI, USA, 2009.